

***Final Draft***  
**of the original manuscript:**

Pearson, J.; Fox-Kemper, B.; Pearson, B.; Chang, H.; Haus, B.; Horstmann, J.;  
Huntley, H.; Kirwan, Jr., A.; Lund, B.; Poje, A.:

**Biases in Structure Functions from Observations of Submesoscale Flows.**

In: Journal of Geophysical Research : Oceans. Vol. 125 (2020) 6,  
e2019JC015769.

First published online by AGU: 22.05.2020

DOI: 10.1029/2019JC015769

<https://dx.doi.org/10.1029/2019JC015769>



## Biases in Structure Functions from Observations of Submesoscale Flows

Jenna Pearson<sup>1</sup> , Baylor Fox-Kemper<sup>1</sup> , Brodie Pearson<sup>2</sup> , Henry Chang<sup>3</sup>, Brian K. Haus<sup>4</sup> , Jochen Horstmann<sup>5</sup>, Helga S. Huntley<sup>3</sup> , A. D. Kirwan Jr.<sup>3</sup>, Björn Lund<sup>4</sup> , and Andrew Poje<sup>6</sup>

### Key Points:

- Structure functions calculated from observed drifters are subject to accumulation bias when compared to those from Eulerian observations
- Structure functions calculated from either drifters or Eulerian data may be subject to a background bias due to mean gradients in the flow
- These biases preclude inferences about energy cascades or fluxes from structure functions from drifters or localized Eulerian data

### Correspondence to:

J. Pearson,  
jenna\_pearson@brown.edu

### Citation:

Pearson, J., Fox-Kemper, B., Pearson, B., Chang, H., Haus, B. K., Horstmann, J., et al. (2020). Biases in structure functions from observations of submesoscale flows. *Journal of Geophysical Research: Oceans*, 125, e2019JC015769. <https://doi.org/10.1029/2019JC015769>

Received 15 OCT 2019

Accepted 13 MAY 2020

Accepted article online 22 MAY 2020

<sup>1</sup>Department of Earth, Environmental and Planetary Sciences, Brown University, Providence, RI, USA, <sup>2</sup>College of Earth, Ocean, and Atmospheric Sciences, Oregon State University, Corvallis, OR, USA, <sup>3</sup>School of Marine Science and Policy, University of Delaware, Newark, DE, USA, <sup>4</sup>Rosenstiel School of Marine and Atmospheric Science, University of Miami, Miami, FL, USA, <sup>5</sup>Helmholtz Zentrum Geesthacht, Geesthacht, Germany, <sup>6</sup>Department of Mathematics, College of Staten Island, City University of New York, Staten Island, NY, USA

**Abstract** Surface drifter observations from the Lagrangian Submesoscale Experiment (LASER) campaign in the Gulf of Mexico are paired with Eulerian (ship-borne X-band radar) data to demonstrate that velocity structure functions from drifters differ systematically from Eulerian structure functions over scales from 0.4 to 7 km. These differences result from drifters oversampling surface convergences and regions of intense vorticity. The first-, second-, and third-order structure functions are calculated using quasi-Lagrangian (drifter) and Eulerian data from approximately the same location and time. Differences between quasi-Lagrangian and Eulerian structure functions are attributed to two forms of bias. The first bias results from the mean divergence or vorticity of the background flow creating nonzero first-order structure functions. This background bias affects both quasi-Lagrangian and Eulerian data when insufficiently time-averaged. It severely biases the drifter third-order structure functions but is smaller in Eulerian structure functions at both second and third order. This bias can be corrected for using lower-order structure functions. The second form of bias results from drifters accumulating in regions with flow statistics that differ from undersampled regions. This accumulation bias is diagnosed by identifying the dependence of the Eulerian structure functions on divergence and vorticity as well as scale. Together, both biases suggest that caution is needed when interpreting second-order drifter statistics and that linking raw third-order drifter statistics to energy fluxes is often erroneous in ocean data: Even with background correction and sufficient time-averaging, drifters overestimate the Eulerian estimate of the third-order structure function by up to a factor of 5 when signs are consistent.

**Plain Language Summary** Structure functions are a statistic used to measure the spreading of material floating in the ocean, such as plastics or spilled oil, as well as the transfer of properties like energy across scales. Their calculation requires knowledge of velocities of nearby particles. These can be measured either by (nearly) stationary instruments, such as a radar, or by tracking drifters. Offshore drifter tracking is generally easier, but they are known to be attracted to specific flow features, such as fronts, windrows, and vortices, leading to less sampling of other areas. By considering a unique data set of nearly simultaneous velocity measurements from both radar and drifters, this paper investigates how the uneven sampling by drifters, as well as the limited area coverage of radar measurements, impacts the structure function statistics and their interpretation.

## 1. Introduction

Surface dispersion of plankton, contaminants, and plastics is largely controlled by the variability of surface currents over a rich array of scales. While absolute dispersion is dominated by mesoscale and larger ( $\geq \mathcal{O}(100 \text{ km})$ ) motion, for relative dispersion, the submesoscales—characterized by horizontal scales of  $\mathcal{O}(0.1 - 10 \text{ km})$ , timescales of hours to days, and  $\mathcal{O}(1)$  Rossby and Richardson numbers—are of particular importance. The equal competition of planetary vorticity with horizontal shear at submesoscales leads to a transition from large quasi-geostrophically balanced motions to smaller forward-cascading turbulence, providing a pathway for dissipation of both energy and tracer variance (McWilliams, 2016; McWilliams et al., 2001). Submesoscale phenomena are pervasive in the mixed layer as seen in observations (Buckingham et al., 2016; Callies et al., 2015; Du Plessis et al., 2019; Johnson et al., 2016; Ohlmann et al., 2017; Omand

et al., 2015; Poje et al., 2014) and suggested by numerical models and theory (Capet et al., 2008, 2008a, 2008b; Fox-Kemper et al., 2008a; Luo et al., 2016; Thomas et al., 2008; Zhong et al., 2012). They are strong contributors to the transfer of energy between scales and energy dissipation (D'Asaro et al., 2011; McWilliams, 2008; Molemaker et al., 2005; Poje et al., 2017) and affect the distribution of biogeochemical variables throughout the near-surface ocean (Klein & Lapeyre, 2009; Li et al., 2012; Mahadevan & Tandon, 2006; Zhong et al., 2012; Omand et al., 2015). Although ubiquitous, submesoscale turbulence is difficult to detect with most observational platforms due to limited resources, remoteness, and the ephemeral nature of submesoscale currents (D'Asaro et al., 2011, 2018; McWilliams, 2016). Lagrangian instruments are well suited for this purpose because they approximately follow currents at depth (Davis, 1991; Riser, 1982) and at the surface (Novelli et al., 2017) on submesoscale timescales, and thus targeted deployments of Lagrangian instruments are capable of capturing the spatiotemporal evolution of the fronts, eddies, and filaments associated with the submesoscale.

Drifters provide a low-cost measurement platform with the potential for high resolution in both space and time, but they have a tendency to cluster in regions of convergence associated with horizontal density gradients and cyclonic vorticity (Chang et al., 2019; Choi et al., 2017; D'Asaro et al., 2018; Pearson et al., 2019). Numerical simulations of the Northern Gulf of Mexico by Choi et al. (2017) and Pearson et al. (2019) show that impacts of this biased sampling on turbulence statistics are strongest in the submesoscale. At scales less than 30 km, large releases of  $\sim 30,000$  synthetic drifters produced shallower second-order structure functions and larger third-order structure functions than Eulerian structure functions calculated using the model grid. Individual releases of clusters of synthetic drifters ( $\sim 300$ – $1000$ ) to emulate previous drifter launches in the Gulf of Mexico were also analyzed. The structure functions from cluster releases were similarly shallow and large for second- and third-order structure functions respectively but much more variable across scales. Divergence and vorticity structure functions suggest that coherent and correlated submesoscale features are responsible for different Eulerian and drifter statistics, findings that can now be verified with observations from the Lagrangian Submesoscale Experiment (LASER) in winter of 2016.

LASER generated both Eulerian and quasi-Lagrangian surface velocity observations, in the form of shipboard X-band radar measurements (Lund et al., 2018) and GPS-tracked drifters drogued at 60 cm (D'Asaro et al., 2018; Novelli et al., 2017). The drifters are only “quasi-Lagrangian” as they are confined to the surface and therefore do not capture the full 3-D velocity field in the true Lagrangian sense. Thus, throughout this paper, “convergences” in the drifter trajectories do not imply 3-D convergence, only surface convergence. Simultaneous and colocated Eulerian and quasi-Lagrangian measurements are rare, and this is the first experiment we know of where the measurements are close enough and dense enough in space and time to provide comparable statistics. See section 2 for more details.

Structure functions are a common tool for quantifying dispersion properties of fluid flows and placing the statistics into the context of turbulence theory. Following Pearson et al. (2019), differences between Eulerian and Lagrangian structure functions are investigated through an analysis of the impact of specific flow conditions on the statistics. These methods are described in section 3. Section 4 describes the results, and discussion and conclusions follow in section 5.

## 2. Data

### 2.1. LASER Drifters

Roughly 1,000 GPS-tracked CARTE-type surface drifters (Novelli et al., 2017) were released in the Northern Gulf of Mexico as a part of the LASER between 18 January and 13 February 2016 (see Figure 1a). These drifters were specifically engineered to be cheap, easy to assemble, and biodegradable to reduce pollution. They reported position data nominally every 5 min for several months and were drogued to follow the integrated flow of the top 60 cm of the water column (Novelli et al., 2017). Tank experiments show the drifters are subject to less than 0.5% windage at 10-m wind speeds of 8–23 m/s (Novelli et al., 2017). The drifter trajectories were processed by removing outliers, low-pass filtering (Yaremchuk & Coelho, 2015), and interpolating positions to uniform 15-min intervals. Some of the drifters lost their drogues during or following deployment, and the data following drogue-loss were discarded, based on the drogue-loss detection method of Haza et al. (2018).

To examine sampling bias caused by different local flow regimes, we consider separately three groups of observations across four deployments (one group combines two deployments). The three groups are denoted

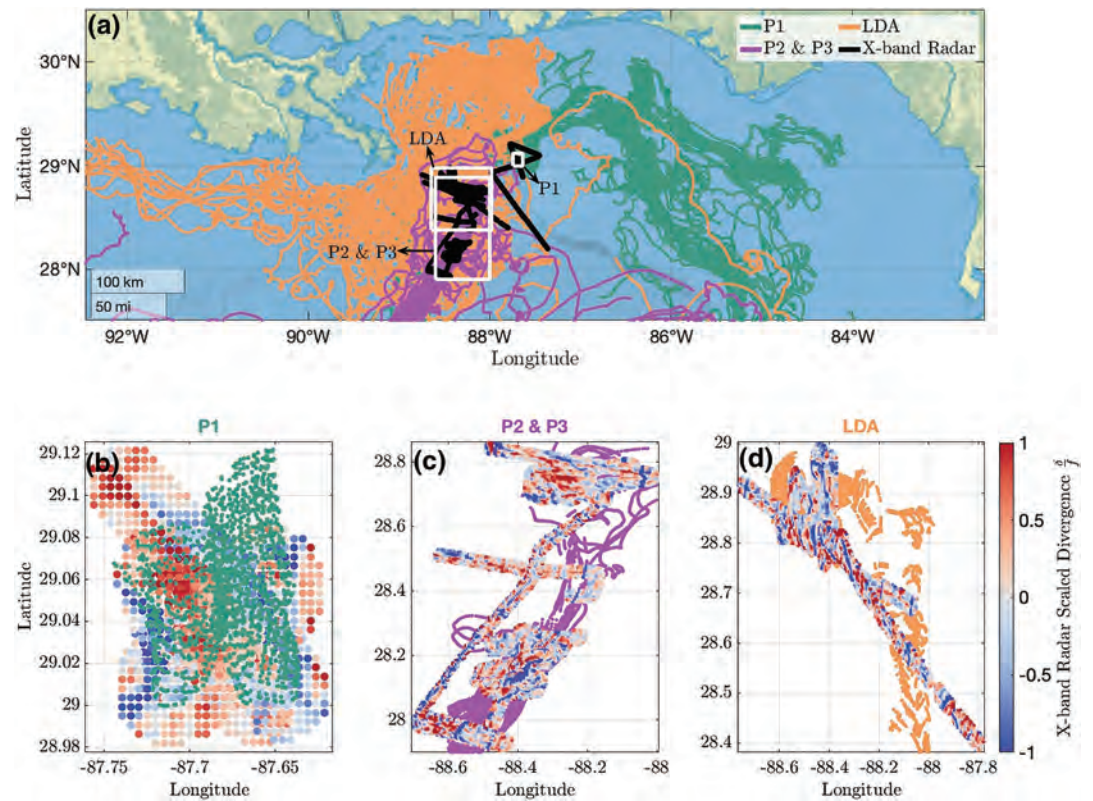


**Figure 1.** (a) Trajectories for the P1 (green), P2 & P3 (pink), and LDA (orange) drifter deployments. The shiptrack X-band radar footprint is shown in black. To ensure the best overlap between the two data sets, the drifters and X-band measurements were analyzed only in the indicated domains and the time-frames shown in Table 1. (b–d) Scaled divergence  $\Delta/f$  from X-band radar for the time frames and domains for (b) P1, (c) P2 & P3, and (d) LDA.

“P1,” “P2 & P3,” and “LDA.” P1 was a deployment of 300 drifters in a cloverleaf pattern over an  $8\text{ km} \times 8\text{ km}$  region with submesoscale activity and a modest horizontal density gradient, east of the freshwater front from the Mississippi River, on 21 January 2016. LDA was a deployment of 326 drifters on an approximately uniform grid over a  $20\text{ km} \times 20\text{ km}$  region targeting a vortex identified in satellite images and aerial sea surface temperature maps on 7 February 2016 (D’Asaro et al., 2018). This launch overlapped more substantially with the ship-track data than other available launches (see Figure 1). Lastly, P2 & P3 were distributed drifter releases from 25 January through 31 January 2016 (265 drifters in all) targeting submesoscale fronts, filaments, and Langmuir circulation. This group samples conditions when frontogenesis is the primary feature.

## 2.2. X-Band Radar

A Doppler (coherent-on-receive) marine X-band radar developed by Helmholtz Zentrum Geesthacht (HZG), Geesthacht, Germany, was installed on the *R/V Walton Smith* in support of LASER. It consisted of a commercial GEM elettronica marine X-band (9.4 GHz) radar with a 2.3 m long HH-polarized antenna and a scanning period of 2 s. The antenna was situated at a height of  $\sim 12.5$  m above the sea surface with an unobstructed view in all directions. The radar transceiver operates with 12 kW output power and a pulse repetition frequency of 2 kHz in short pulse mode (i.e., a pulse length of 50 ns). The corresponding range and azimuthal resolutions are 7.5 m and  $0.8^\circ$ , respectively. The radar was modified by HZG to measure both intensity and phase of the radar backscatter signal from the sea surface (Braun et al., 2008). The raw, uncalibrated radar measurements are linearly amplified and digitized at 20 MHz with 13-bit precision per channel. The A/D converter and amplifier are located inside the radar transceiver. The system samples the radar backscatter signal up to a maximum range of  $\sim 3.1$  km.

The X-band radar backscatter from the sea surface is due to a combination of Bragg scattering (Barrick & Peake, 1968; Wright, 1968) and sea spikes associated with wave breaking (Trizna et al., 1991; Wetzel, 1990).

**Table 1**  
*Data Windows*

Launch	Time frame	No. of drifters	Features sampled
P1	21 January 2016, 13:51:04 to 21 January 2016, 19:08:39	300	Submesoscale activity, modest density front
P2 & P3	26 January 2016, 00:16:44 to 01 February 2016, 19:40:23	197	Submesoscale fronts, filaments, and Langmuir circulation
LDA	07 February 2016, 02:47:41 to 12 February 2016, 19:40:50	326	Vortex

This study uses near-surface current vectors derived from the long (>15 m) surface wave signal within the X-band radar backscatter intensity imagery. Surface waves appear as bands of enhanced and weakened backscatter primarily due to tilt modulation, that is, wave-induced changes to the local incidence angle (Lyzenga & Walker, 2015; Støle-Hentschel et al., 2018). Additional wave imaging mechanisms are partial shadowing and hydrodynamic modulation (Nieto Borge et al., 2004). The ship-motion-corrected and georeferenced radar backscatter intensity measurements were partitioned into evenly distributed and partially overlapping circular analysis windows with a radius of 480 m and 30 min periods, with the actual number of data points per analysis window and period depending on the ship track. We note that smoothing from overlapping analysis windows lowers the total variability and may affect scales below 1 km. While comparison with tests from synthetic data suggests this contribution is likely small, a more detailed analysis of the effects of overlap size is necessary to account for the full effects and will be investigated in future studies.

Simultaneous georeferenced measurements in a field of view surrounding the ship allow the radar data to be interpreted as an Eulerian field of near-continuous observations. The methodology employed here is based on the well-established 3-D Fourier transform technique, which identifies the wave-related wavenumber-frequency coordinates within a radar image power spectrum, and then solves for the current vector by minimizing the wave coordinates' distance from the linear wave dispersion relationship (Senet et al., 2001; Young et al., 1985). The effective depth of the resulting current vector depends on the lengths of the underlying surface waves (Campana et al., 2017; Lund et al., 2015). Here, the currents are based on ocean wavenumbers ranging from 0.1–0.3 rad m<sup>-1</sup>, which corresponds to an approximate effective depth of 1–5 m (Stewart & Joy, 1974). Based on a comparison between the X-band radar and CARTHE drifter measurements analyzed here, the X-band radar currents have an accuracy better than 0.04 m s<sup>-1</sup> in terms of speed and 12° in terms of direction. For additional details on the X-band radar processing and validation, the reader is referred to Lund et al. (2018).

### 2.3. Data Windows

To ensure robustness of the statistics, windows in space and time were chosen that were densely sampled by drifters and the X-band radar. These are summarized in Table 1. The geographic domains for each launch group are shown in Figure 1. The drifter times were also constrained to match the time step of the Eulerian data by taking the nearest available drifter measurement for each Eulerian time step. These data subsets were used for the structure function analysis presented in sections 4.1 and 4.2.1. For the joint probability density function and structure function dependent on scale and divergence or vorticity presented in section 4.2.2, all available X-band radar data were used covering the domain (lat ∈ [27.9049, 29.2305], lon ∈ [−88.7640, −87.3916], time ∈ [20 January 2016, 15:56:10, 12 February 2016, 19:40:50]). Additionally, the structure functions of both drifters and X-band radar were compared for two individual snapshots of a front on 31 January 2016, 12:16:19, and a vortex on 12 February 2016, 6:00:59.

## 3. Methods

### 3.1. Structure Functions

Velocity structure functions are the moments of velocity increments between two points and provide information about the properties of turbulent dynamics at different scales. Given two drifters, the velocity components of interest are those projected onto the longitudinal (along-separation) and transverse (cross-separation) directions. If the positions of a pair of drifters are  $(x_1, y_1)$  and  $(x_2, y_2)$ , then the horizontal separation vector between them is given as  $\mathbf{r} = \Delta x \hat{\mathbf{i}} + \Delta y \hat{\mathbf{j}}$ , where  $\Delta x = x_2 - x_1$ ,  $\Delta y = y_2 - y_1$ . The

drifter positions can be rewritten in terms of the separation vector,  $\mathbf{r}$ , by letting  $(x_1, y_1)$  correspond to  $\mathbf{x}$  and  $(x_2, y_2)$  correspond to  $\mathbf{x} + \mathbf{r}$ . The longitudinal velocity increment is the projection of  $\Delta \mathbf{u} = \mathbf{u}(\mathbf{x} + \mathbf{r}) - \mathbf{u}(\mathbf{x})$  in the direction of  $\mathbf{r}$  and given by  $\Delta u_L = (\mathbf{u}(\mathbf{x} + \mathbf{r}) - \mathbf{u}(\mathbf{x})) \cdot \hat{\mathbf{r}}$ . The transverse velocity increment is perpendicular to both  $\mathbf{r}$  and the local vertical  $\hat{\mathbf{k}}$  and is given by  $\Delta u_T = \hat{\mathbf{k}} \cdot ((\mathbf{u}(\mathbf{x} + \mathbf{r}) - \mathbf{u}(\mathbf{x})) \times \hat{\mathbf{r}})$  or equivalently  $\Delta u_T = (\hat{\mathbf{r}} \times \hat{\mathbf{k}}) \cdot (\mathbf{u}(\mathbf{x} + \mathbf{r}) - \mathbf{u}(\mathbf{x}))$ . These increments are used to construct the isotropic and homogeneous  $n$ th-order structure function, defined as

$$S_\gamma^n(r) = \langle (\Delta u_\gamma)^n \rangle, \quad (1)$$

where  $\langle \cdot \rangle$  is an ensemble or spatiotemporal average,  $n$  is the order of the structure function (or equivalently the  $n$ th raw statistical moment of the velocity increment field), and  $\gamma$  refers to the velocity components (either longitudinal [L] or transverse [T]).

While equation (1) can be constructed with any value of  $n$ , it is the second- and third-order ( $n = 2, 3$ ) structure functions that are most commonly analyzed and relevant in turbulence studies. Note that the higher the moment, the more sensitive it is to the tails of the distribution. Thus, with limited sampling, the higher-order statistics are noisier and harder to estimate than the lower-order statistics. The second-order structure function, which is the variance of the velocity increments, is related to the kinetic energy spectrum through a Fourier cosine transform (Webb, 1964). This results in a linear relation between the respective slopes of structure functions and spectra (McCaffrey, Fox-Kemper, & Forget, 2015), provided the spectral slopes fall between -1 and -3 (Babiano et al., 1985). Spectral power law predictions for different turbulent regimes can therefore be transcribed to make structure function predictions for these regimes (Babiano et al., 1985; Bennett, 1984; Callies & Ferrari, 2013; LaCasce, 2008), even when multiple power laws are present at different scales as is sometimes the case for geophysical flows (Frehlich & Sharman, 2010; McCaffrey, Fox-Kemper, Hamlington, & Thomson, 2015; Pearson et al., 2019). In this paper, guidelines comparing theoretical structure function slopes for particular classical cascade theories will be provided by dashed gray lines alongside observed structure functions, but these are provided only for reference: Power spectra are poorly constrained by drifters (LaCasce, 2016). We evaluate the biases of structure functions regardless of whether conversions between spectra and structure functions are possible (per Babiano et al., 1985). Third-order structure functions may offer information about energy transfer between scales and, when paired with first- and second-order structure functions, provide a more complete classification of turbulence statistics. The details of relevant third-order structure function theories can be found in Lindborg (1999, 2007), Pearson et al. (2019), and Poje et al. (2017).

In homogeneous flows, statistics do not vary from location to location. This implies the mean velocity must be constant and there are no mean gradients of scalars or vectors in the flow. Consequently, the first-order structure function is zero. As a result, there is no distinction between the *central* moments and the *raw* moments of the velocity increments as calculated using equation (1) for homogenous turbulence. In isotropic turbulence, the statistics have no preferred directionality, implying there can be no mean vectors. With this restriction, even a constant mean velocity is disallowed.

However, heterogeneous flows with a stationary “mean” current that varies in space can be decomposed as  $\mathbf{u}(\mathbf{x}, t) = \overline{\mathbf{u}}(\mathbf{x}) + \mathbf{u}'(\mathbf{x}, t)$ , where the overline denotes a temporal average. The structure functions then depend on both the mean and fluctuating velocity components [ $S_\gamma^n(r) = \langle (\Delta u_\gamma)^n \rangle = \langle (\Delta \overline{u}_\gamma + \Delta u'_\gamma)^n \rangle$ ], where  $\langle \cdot \rangle$  denotes a *spatiotemporal* or *ensemble* average (without this average the velocity increments depend on both position and separation distance). The presence of a mean current  $\overline{u}(\mathbf{x})$  can result in a nonzero first-order structure function ( $S_\gamma^1 \neq 0$ ), even when the fluctuating flow satisfies  $\langle \Delta u' \rangle = 0$ .

For example, when the longitudinal first-order structure function is positive, the background flow has mean divergence. Similarly, a positive transverse first-order structure function implies a counterclockwise background flow. If the first-order longitudinal and transverse structure functions are negative, it indicates a background flow with average convergence and clockwise rotation, respectively. Figure 2 illustrates these kinematic effects. Note that in the general definition,  $\Delta u_{\gamma_1} = u_{\gamma_2} - u_{\gamma_1}$ , where  $\gamma$  is any velocity component, and we wish to evaluate the effect on the longitudinal ( $u_L$ ) and transverse ( $u_T$ ) components through projection of the Cartesian meridional ( $u_y$ ) and zonal ( $u_x$ ) velocities given as  $\Delta u_L = (\Delta u_x \Delta x + \Delta u_y \Delta y)/r$  and  $\Delta u_T = (-\Delta u_x \Delta y + \Delta u_y \Delta x)/r$ .

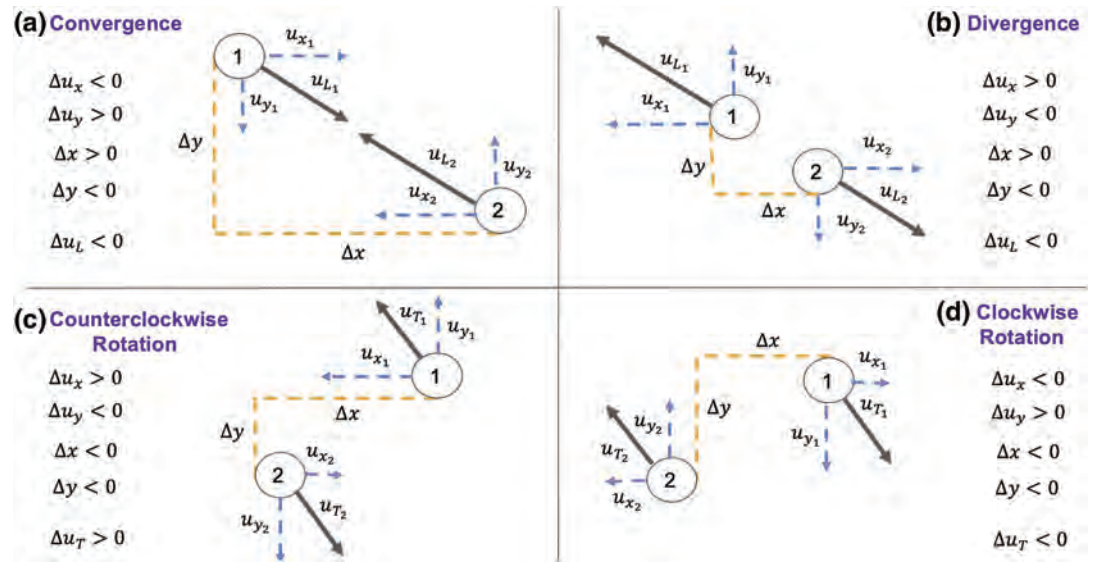


**Figure 2.** Demonstration of the relationship between the first-order structure function and drifters subject to (a) convergent flow, (b) divergent flow, (c) counterclockwise rotation, and (d) clockwise rotation. When subtracting the variables of the second drifter from the first (an arbitrary choice), the sign of the first-order structure function is determined. The signs of the differences that go into forming the  $S_L^1 = \langle \Delta u_x \Delta x + \Delta u_y \Delta y \rangle$  and  $S_T^1 = -\Delta u_x \Delta y + \Delta u_y \Delta x$  are provided.

Under the above heterogeneous flow decomposition, the first-order structure function calculated by equation (1) is related algebraically to the second- and third-order statistics by

$$\begin{aligned} \langle (\Delta u_y)^2 \rangle &= \langle (\Delta \bar{u}_y)^2 + 2\Delta \bar{u}_y \Delta u'_y + (\Delta u'_y)^2 \rangle \\ &\approx \langle \Delta \bar{u}_y \rangle^2 + \langle (\Delta u'_y)^2 \rangle, \end{aligned}$$

$$\begin{aligned} \langle (\Delta u_y)^3 \rangle &= \langle (\Delta \bar{u}_y)^3 + 3(\Delta \bar{u}_y)^2 \Delta u'_y + 3\Delta \bar{u}_y (\Delta u'_y)^2 + (\Delta u'_y)^3 \rangle \\ &\approx \langle \Delta \bar{u}_y \rangle^3 + 3 \langle \Delta \bar{u}_y \rangle \langle (\Delta u'_y)^2 \rangle + \langle (\Delta u'_y)^3 \rangle \\ &\approx \langle \Delta \bar{u}_y \rangle^3 + 3 \langle \Delta \bar{u}_y \rangle \left[ \langle (\Delta u_y)^2 \rangle - \langle \Delta \bar{u}_y \rangle^2 \right] + \langle (\Delta u'_y)^3 \rangle \\ &\approx 3 \langle \Delta \bar{u}_y \rangle \langle (\Delta u_y)^2 \rangle - 2 \langle \Delta \bar{u}_y \rangle^3 + \langle (\Delta u'_y)^3 \rangle. \end{aligned}$$

These corrections are exact when the mean flow varies linearly in space. Under more general flow conditions, the corrections negate the leading-order effect of mean flow on the total structure functions provided the Taylor series of  $\bar{u}(\mathbf{x} + \mathbf{r})$  is dominated by the lowest order derivative terms.

Thus, when the perturbation statistics are subdominant, the nonzero first-order structure function can determine the sign and magnitude of the third-order structure function (if the first terms on the right side are much larger than the second) and can determine the magnitude of the second-order structure function. In this paper, these effects are termed *background biases*, to indicate that the background flow biases the uncorrected structure function statistics. To isolate the central (i.e., with the mean removed) moments when the mean increment is nonzero due to background flow, the *corrected structure function*,  $S_y^m(r) = \langle (\Delta u'_y)^m \rangle$ , is defined by the following equations to find the centralized distributions for the perturbation field statistics, which may then be potentially homogeneous and isotropic even if the background flow is not,

$$S_y^2(r) = \langle (\Delta u_y)^2 \rangle - \langle \Delta \bar{u}_y \rangle^2 = S_y^2(r) - [S_y^1(r)]^2, \quad (2)$$

$$S_y^3(r) = \langle (\Delta u_y)^3 \rangle - 3 \langle \Delta \bar{u}_y \rangle \langle (\Delta u_y)^2 \rangle + 2 \langle \Delta \bar{u}_y \rangle^3 = S_y^3(r) - 3S_y^1(r)S_y^2(r) + 2[S_y^1(r)]^3. \quad (3)$$

The use of a flow decomposition implies that there is a meaningful dynamical distinction between the background and perturbation fields. The further assumption that the energy transfer across scales is dominated by the perturbations, justifying the focus on the second- and third-order statistics of the perturbation fields (without the mixed background-perturbation and background-background nonlinear interaction terms), also implicitly assumes a scale, organizational, or amplitude separation between the mean and the perturbation fields. The idealization in this approach, then, is similar to that used in boundary layer turbulence, where mean shear leads to shear production energizing the perturbation fields which then transfer energy across scales, but that the transfer across scales of the mean field by the mean field is negligible. If this assumption holds, then the standard derivations of the energy transfer terms via the Karman-Howarth equation (e.g., Frisch, 1995; Kolmogorov, 1941) are readily constructed from the perturbation equations instead of the total equations, retaining the background-perturbation shear production terms as a source in the perturbation equations (and a sink in the background equations) and assuming the background-background interactions are negligible in transfers across scales. Alternatively, one might choose not to distinguish between background and perturbation fields and using the total flow structure function. However, as the background field is neither homogeneous nor isotropic, this limits the applications of this approach. For example, the Karman-Howarth equation that relates the structure functions to the energy transfer across scales fails at the outset when considering heterogeneous, isotropic structure functions. The total flow structure function may be useful as a statistical descriptor of the flow (albeit a very high dimensional one), but most existing theory cannot be reconciled with this statistic. Frisch (1995) notes that there is an anisotropic generalization of the Karman-Howarth equation in earlier works by Monin and Yaglom, but pursuing this approach is not feasible with the limited set of observations here.

### 3.2. Computational Details

At each time, a structure function is found across all available scales. This is accomplished by binning the velocity increments from individual pairs at the given time-step into logarithmically defined separation scale bins with width 0.2 and averaging over all pairs in each bin. For data windows with multiple time steps, these structure functions were then averaged over time, excluding any bin with less than 10 measurements to ensure the robustness of the statistics. The 95% bias corrected and accelerated confidence interval of the time-mean is found by bootstrapping with 10,000 resamples. For the specific snapshots of a front (sections 4.2.3 and 4.3.3) and vortex (sections 4.2.4 and 4.3.4), the structure function at the single time-step is calculated across all scales and binned in the same fashion, except that no time-averaging is done and the bootstrapped bias corrected and accelerated confidence intervals are found using all the data at each scale from the single time step with 10,000 resamples. For the joint probability distributions and the structure function dependent on divergence and vorticity (sections 4.2.2 and 4.3.2), the divergence and vorticity are averaged over each pair that enters the structure function calculation.

## 4. Results

### 4.1. First-Order Structure Functions

The first-order velocity structure functions (denoted  $S_\gamma^1$ ) are plotted in the upper panels of Figure 3. A detectable background flow is indicated by nonzero values in either the longitudinal or transverse components for all samples, except the P1 drifters. Unlike the other deployments, these were not targeted at a strong flow feature, and because of the relatively short sample window for P1 (see Table 1), the drifters did not converge on an individual flow feature, resulting in more homogeneous sampling.

The only drifter deployment that shows a statistically significant nonzero longitudinal first-order structure function is P2 & P3, which was intentionally launched to sample frontal regions:  $S_L^1$  is generally negative, though small, suggesting convergence. For 6.4 km and above, however, it is positive, indicating divergence. The change in sign identifies a scale at which drifters no longer cluster but are drawn into neighboring convergence zones. See also the related discussion in section 4.2.3, which presents results on a single front with no accompanying sign-change in  $S_L^1$ .

Both P2 & P3 and LDA drifters show a positive  $S_T^1$  across all scales, indicative of counterclockwise rotation. For P2 & P3,  $S_T^1$  is small compared to LDA. The larger values for the LDA drifters reflect the targeted vortex structure. Individual drifter tracks also trace out the counterclockwise vortex of LDA repeatedly, resulting in loops (cf. Griffa et al., 2008).

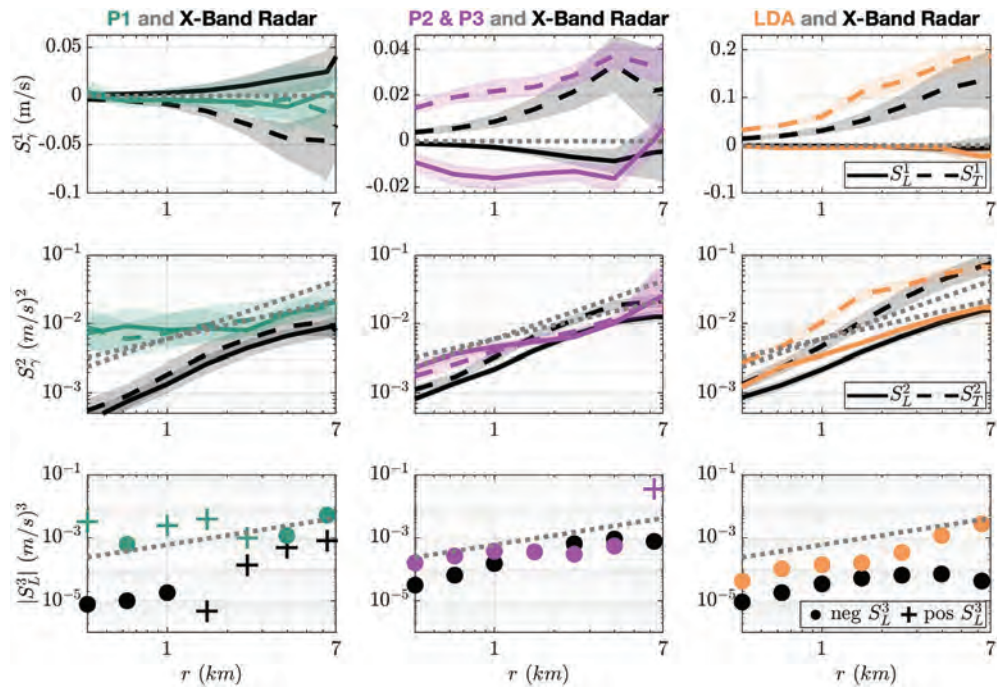


**Figure 3.** The (top row) first-order and (middle row) second-order longitudinal (solid) and transverse (dashed) velocity structure functions, and (bottom row) the absolute values of negative (circle) and positive (plus) third-order longitudinal velocity structure function values for the P1 (left), P2 & P3 (middle), and LDA (right) launches. The drifter deployments are given by the colored lines and symbols and the corresponding Eulerian X-band radar data by the black lines and symbols. Bootstrapped 95% bias corrected and accelerated confidence intervals for the time mean of the first- and second-order structure functions are provided as shading around each line. Dashed gray guidelines through zero are shown in the upper panels. Dashed gray guidelines for the middle panels correspond to theoretical second-order structure function slopes in 3-D ( $2/3$ ) and frontogenesis or an internal gravity wave field ( $1$ ). A guideline of slope  $1$  is also shown for the lower panels for the linear slope of the third-order structure function predicted in the energy cascade region of 3-D, 2-D, or QG turbulence. Notice the difference in the y axes for the first- and third-order structure functions.

In the first-order velocity structure function, quasi-Lagrangian and Eulerian statistics are overall consistent, with a few exceptions in the P1 domain. The X-band radar yields positive  $S_L^1$  for scales above 4 km, consistent with the strong divergence seen in the domain given in Figure 1b. Eulerian  $S_T^1$  for scales between 1 and 6 km is negative, making this the only data set where clockwise rotation dominates on average. These discrepancies within the smallest domain, where sampling by both drifters and X-band radar appears to be spatially most uniform (Figure 1), points to the challenges with obtaining unbiased samples.

#### 4.2. Second-Order Structure Functions

The second-order velocity structure functions are plotted in the middle row of Figure 3. Pearson et al. (2019) found that the second-order structure function slopes derived from a large gridded synthetic drifter release in a model were on average shallower than the Eulerian structure functions computed on the model grid on scales below 10 km. The authors attribute this shallowness to oversampling of convergence regions, consistent with previous studies (Choi et al., 2017; D'Asaro et al., 2018). The results in Figure 3 (middle row) compound the *accumulation* bias from drifters oversampling convergent regions with the *background* bias from nonzero first-order structure functions, shown in both Eulerian and quasi-Lagrangian structure functions, particularly in the transverse component. Here the compounded effects of both biases are discussed, and in sections 4.2.1 and 4.2.2, the effects of the background and accumulation biases respectively will be isolated and discussed.

The Eulerian second-order structure functions, both transverse and longitudinal, are similar across all three sampling windows, with slopes around 1 or somewhat steeper. Only in the LDA sampling period is the transverse component noticeably steeper than the longitudinal component. Such steep slopes are consistent with the model results for Eulerian statistics of Pearson et al. (2019). The results for the quasi-Lagrangian

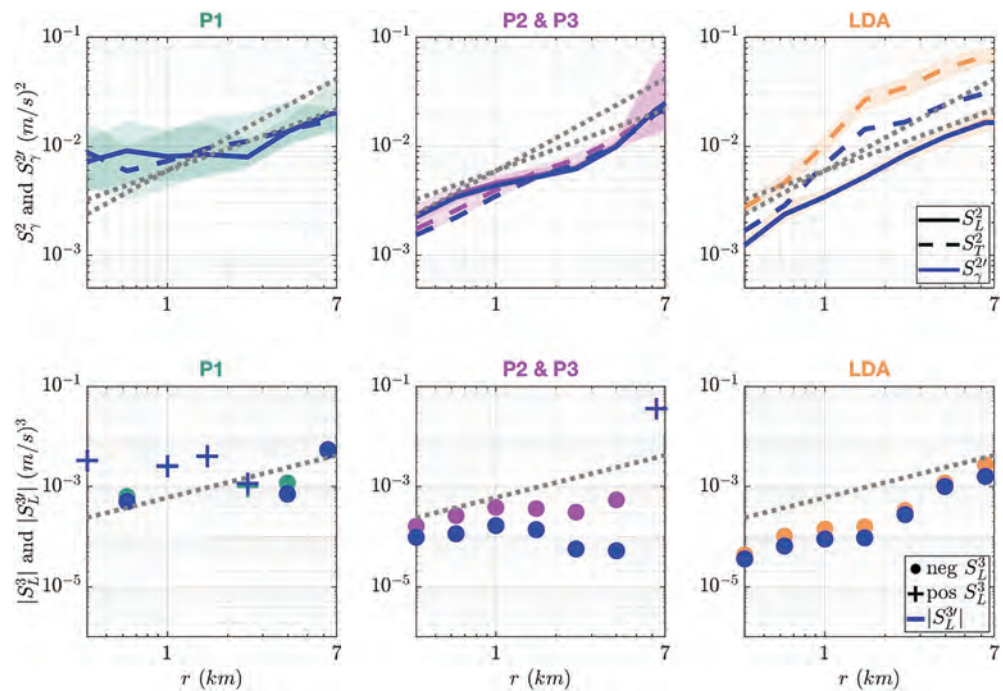


**Figure 4.** The quasi-Lagrangian second-order (upper row) and third-order (lower row) structure functions (green, pink, and orange) and corrected structure functions (blue) from P1 (left), P2 & P3 (middle), and LDA (right) drifter data. Confidence intervals and guidelines are the same as in Figure 3.

calculations are not as consistent. P2 & P3 and LDA drifters exhibit slopes in both transverse and longitudinal second-order structure functions around  $2/3$ , thus somewhat shallower than the Eulerian estimates and consistent with the preferential sampling of convergence zones by these drifters. However, P1 drifters show very little scale dependence at all, much different than the slope of  $2/3$  found in Pearson et al. (2019), and likely due to the small window of time and spatial domain considered here. The disconnect between drifter-derived and radar-derived second-order structure functions for P1 demonstrates that the more uniform sampling in space by the drifters does not suffice to emulate Eulerian sampling, nor does a short time window.

#### 4.2.1. Corrected Second-Order Structure Functions

The second-order structure functions corrected for background bias,  $S_T^{2'}$ , (cf. equations (2) and (3)) are plotted in blue in the upper panels of Figures 4 and 5 alongside the uncorrected structure functions with matching line styles. Most of the second-order corrected and uncorrected structure functions agree within uncertainty intervals, indicating a negligible background flow effect within the limits of detection of our method. The exceptions are the LDA launch, where the quasi-Lagrangian transverse second-order structure function is reduced in magnitude well outside the confidence intervals of  $S_T^2$  and the Eulerian one lies at the outer limit of the confidence interval. Thus, ignoring the background flow for the longitudinal second-order structure functions may be appropriate in ocean surface submesoscale flows, but the transverse structure functions are more prone to bias from background flow effects.

#### 4.2.2. $S_T^2$ as a Function of Divergence and Vorticity

The differences between the quasi-Lagrangian and Eulerian structure functions are not predominantly due to the background bias, an effect of mean divergence or vorticity, as established above. The features oversampled by the drifters (e.g., fronts and vortices) must have fundamentally different structure functions than the domain as a whole, amounting to an accumulation bias. To further diagnose this accumulation bias, we investigate how  $S_T^2$  varies with divergence and vorticity. For this purpose, the complete time series of Eulerian radar data (see section 2.3) is analyzed. The (uncorrected) second-order structure function is computed as a function of both separation distance  $r$  and divergence ( $S_T^2(r, \Delta)$ ), then of  $r$  and vorticity ( $S_T^2(r, \zeta)$ ). The uncorrected structure function values were chosen in lieu of the corrected values for direct comparison with other uncorrected structure functions in the literature (including the results of Pearson et al., 2019), as well as the relatively small first-order structure function dependent on separation from all available

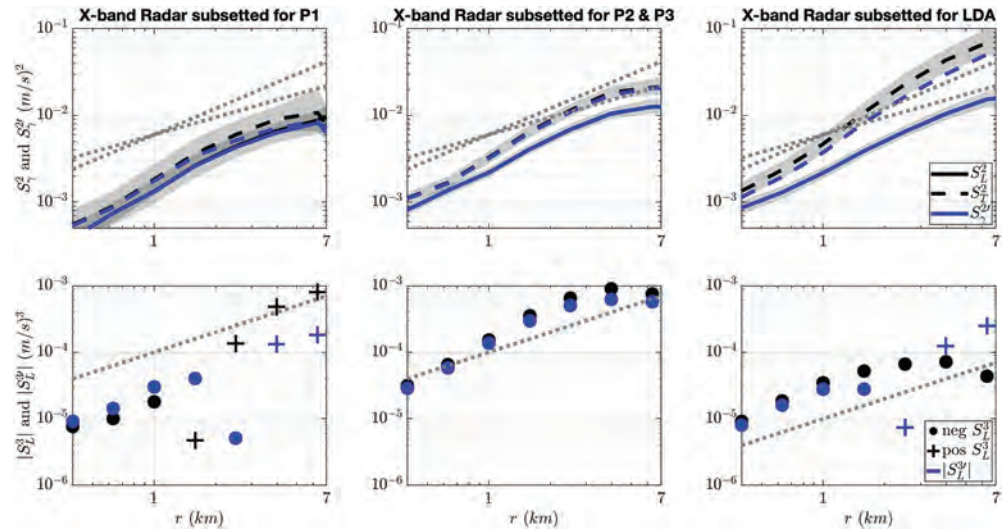


**Figure 5.** The X-band second-order (upper row) and third-order (lower row) structure functions (black) and corrected structure functions (blue) in the P1 (left), P2 & P3 (middle), and LDA (right) domains. Confidence intervals and guidelines are the same as in Figure 3.

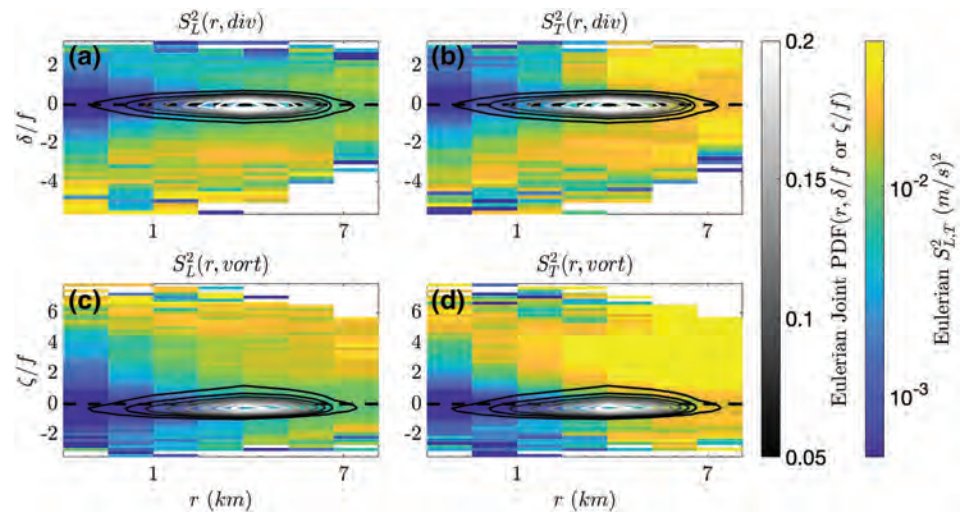
X-band measurements (not shown). This is complimentary to the results of Figure 5, where the correction for X-band measurements is generally within confidence intervals of the uncorrected structure functions even for subsetted data.

Figure 6 shows the results in the yellow-blue colored field. Overlaid with black-white contours are the joint probability density functions (JPDFs) of divergence and separation distance (top) and of vorticity and separation distance (bottom) to show the sampling distribution. Similar to the structure functions of specific launches (Figure 3), both  $S_y^2(r, \Delta)$  of the upper panels and  $S_y^2(r, \zeta)$  of the lower panels show strong dependence on separation distance  $r$ . This is especially true at the most frequently sampled Eulerian divergence and vorticity levels, highlighted by the maxima in the JPDF. Based on the overlaps between the JPDF and the structure function values across scales, the Eulerian structure functions  $S_y^2(r)$  are expected to be steeply sloped. The panels also show that lower divergence and higher vorticity levels (from oversampling regions of strong convergence and counterclockwise rotation) could lead to larger or shallower second-order structure functions.

Below, two specific events are isolated that are characterized by significant convergence and vorticity, respectively. Such strong events are hypothesized to be the primary causes of the different slopes between Eulerian and quasi-Lagrangian structure functions, consistent with the findings of Pearson et al. (2019).

#### 4.2.3. Biases in Second-Order Structure Functions at a Front

The statistics at a front, as observed concurrently on 31 January 2016 with X-band radar and some of the drifters launched during the P2 & P3 deployments, are presented in Figure 7. The front itself is characterized by a strong convergence region near the center of the domain (Figure 7a), as indicated by the blues in the Eulerian divergence field, which reaches values around  $-2f$ . This convergence can also be detected in the drifter velocity field (pink arrows) and in the drifter distribution itself, with many drifters drawn into the frontal region. The western side of the front shows positive vorticity (Figure 7b), with values up to  $2f$ , while weaker negative vorticity dominates the eastern side. The quasi-Lagrangian first-order structure functions are both significantly different from zero and larger than for the full P2 & P3 data set (cf. Figure 3). The signs reflect the drifters' preferential sampling of negative divergence and positive vorticity nearly equally across all scales, consistent with Figures 7a and 7b. The Eulerian field extends farther away from the front than the drifter samples and thus incorporates regions of quite weak divergence and vorticity (Figures 7a and 7b). This leads to the Eulerian  $S_T^1$  being indistinguishable from zero, except at the largest scale. The Eulerian  $S_L^1$ , on the other hand, is only near zero for small scales and significantly negative at large scales (Figure 7c). This is a result of the presence of relatively strong negative divergence in the domain, east of the front, while any positive divergence in the domain is weak (Figures 7a and 7b).



**Figure 6.** Eulerian longitudinal (a, c) and transverse (b, d) uncorrected second-order structure functions as a function of divergence and scale (a, b) and of vorticity and scale (c, d), denoted by the blue to yellow logarithmic colormap. The joint probability density function of divergence and separation distance (a, b) and vorticity and separation distance (c, d) is shown by contours colored using the black to white colormap. Both divergence and vorticity are scaled by the mean Coriolis parameter in the domain.

As previously seen in section 4.2.1 for the larger sample domains, the background bias correction does not significantly alter the second-order structure functions, except at the largest scales, which may not be sampled sufficiently. Both longitudinal and transverse  $S_y^2$  are nearly flat for the drifter data (Figure 7e)—in contrast to the statistics for the full P2 & P3 domain (Figure 4). The Eulerian  $S_y^2$ , on the other hand, exhibit slopes comparable to those from the full P2 & P3 domain (Figure 5) and are therefore much steeper than the quasi-Lagrangian statistics observed directly at the front.

These results are consistent with the discussion in section 4.2.2, considering the divergence and vorticity values being sampled. Figures 6a and 6b show that  $S_y^2$  at an average divergence around  $-2f$  should be relatively flat, although Figures 6c and 6d suggest that for vorticity values near  $2f$ , lower values are expected at the small scales for  $S_L^2$  and to a lesser degree also for  $S_T^2$ . The lack of a slope at small scales in the frontal data indicates that the presence of strong divergence dominates the vorticity in the second-order structure function. Since the small scales of the X-band radar data are less biased toward strong convergence and not biased toward positive vorticity (as is seen both in Figure 7a and 7b and in the Eulerian  $S_y^1$ ), the same flattening of the  $S_y^2$  slopes is not observed in the Eulerian statistics. This is an illustration of the strong impact the accumulation bias in the drifter data can have on the statistics.

#### 4.2.4. Biases in Second-Order Structure Functions in a Vortex

Figure 8 illustrates a different event: a vortex sampled with X-band radar and some of the drifters from the LDA deployment on 12 February 2016. The vortex is characterized by strong positive vorticity everywhere, reaching values up to  $4f$  (Figure 8b). While the domain is generally marked by weak divergence (less than  $1f$ ), it contains small pockets of stronger positive divergence (up to  $3f$ ); see Figure 8b. The sampling by the drifters is strongly nonuniform and takes the shape of a counterclockwise spiral into the vortex.

Figures 8c and 8d, showing the first-order structure functions, suggest that both the X-band radar and drifters tend to sample larger divergence and vorticity at larger scales. Unlike in the frontal example, the corrections for nonzero  $S_y^1$  to  $S_y^2$  are significant for the transverse components. Note that  $S_T^1$  is 2 to 3 times larger here than either  $S_T^1$  or  $S_L^1$  near the front. The impact of background bias on the slope is not clear for the drifters but appears to be flattening for the Eulerian data.

As before, the variability of  $S_y^2$  as a function of vorticity and divergence examined in section 4.2.2 can link the observed slopes to an accumulation bias. The increasing vorticity sampling with increasing scale suggests a diagonal cross section through the fields in Figures 6c and 6d is appropriate, from the left just above zero to the top right, or from low to high  $S_y^2$  values. The increasing divergence sampling with increasing scale reinforces this pattern. Note that the drifters are not in an obvious convergence region in this sample. Nonetheless, the nonuniform sampling of vorticity produces an accumulation bias effect. It is, therefore,

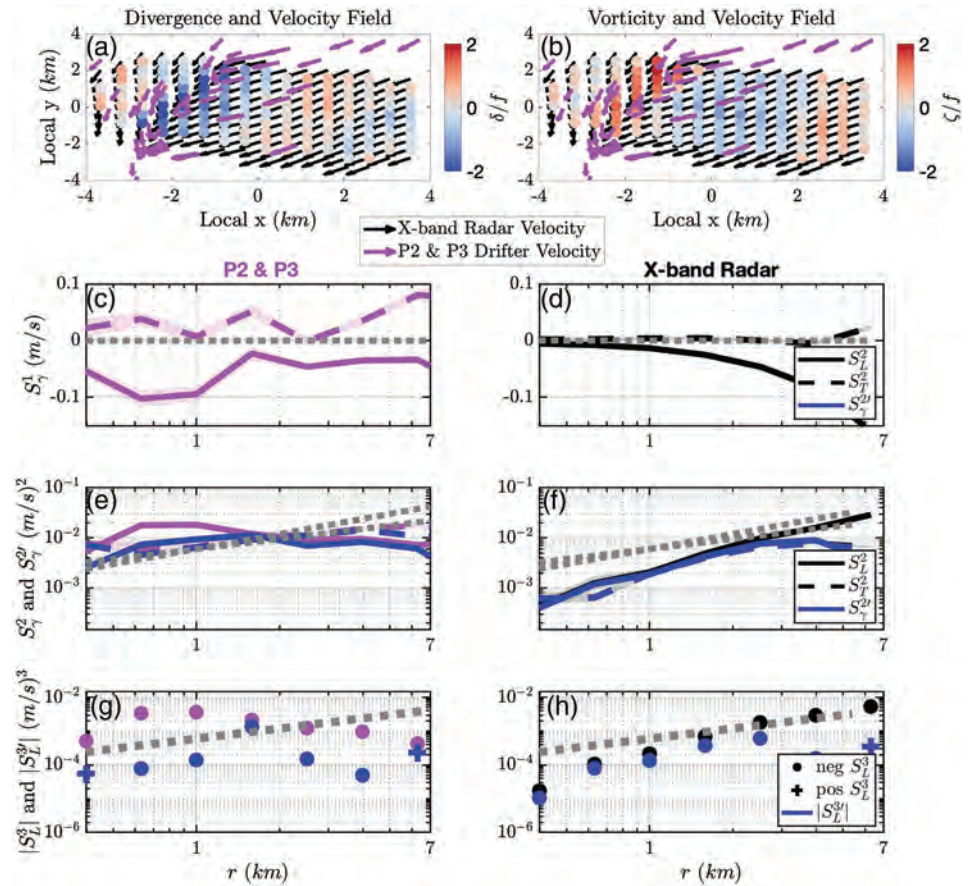


**Figure 7.** (a) The velocity and divergence fields at a front on 31 January 2016 at 12:16:19 UTC. Eulerian velocities are given by black arrows and the P2 & P3 velocities by the pink arrows. Underlain is the Eulerian divergence field scaled by  $f$ . (b) Same as panel (a) but with the scaled vorticity field instead of divergence. P2 & P3 drifter (left) and corresponding X-band (right) (c, d) first-order, (e, f) second-order, and (g, h) third-order structure functions. The corrected second- and third-order structure functions are given by the blue markers in panels (e)–(h). Negative and positive values for the third-order structure functions are plotted with dots and pluses, respectively. The 95% bias corrected and accelerated confidence intervals are shown with shading. Note that these confidence intervals are formed from the mean value at a given scale for this particular snapshot. Guidelines are the same as in Figure 3.

important to keep in mind over what variety of flow fields the structure functions are computed when interpreting them.

### 4.3. Third-Order Structure Functions

The third-order longitudinal structure function,  $S_L^3$ , is plotted in the lower panels of Figure 3 for the drifters and the X-band radar data available during each launch. In contrast to the second-order structure function, the third-order structure function is not positive definite, so the absolute value is plotted with symbols denoting negative ( $\bullet$ ) or positive ( $+$ ) values. Confidence intervals are not plotted, but the quasi-Lagrangian estimates fall mostly outside the 95% confidence window for Eulerian data below 2 km for P1 and P2 & P3. The exception is the LDA deployment, for which only the largest scale falls outside Eulerian confidence intervals. Even so, the LDA drifter  $S_L^3$  exceeds the X-band radar  $S_L^3$  by a factor of 3 to 5, especially over the middle range of scales where the structure functions tend to be most reliable due to adequate sampling. In terms of sign, both the quasi-Lagrangian and the Eulerian structure functions are consistently negative in the LDA domain. The same is true of the Eulerian  $S_L^3$  in the P2 & P3 domain, but here the quasi-Lagrangian  $S_L^3$  changes sign above 5 km. For P1, the Eulerian third-order structure function changes sign at about 1.5 km, but the drifter-based statistics do not have a single clear transition from negative to positive  $S_L^3$ . The slopes for the Eulerian estimates for P2 & P3 and for LDA are somewhat steeper than 1.  $S_L^3$  of the corresponding drifter launches are more variable across scales, but the slope for the LDA launch is comparable, while that

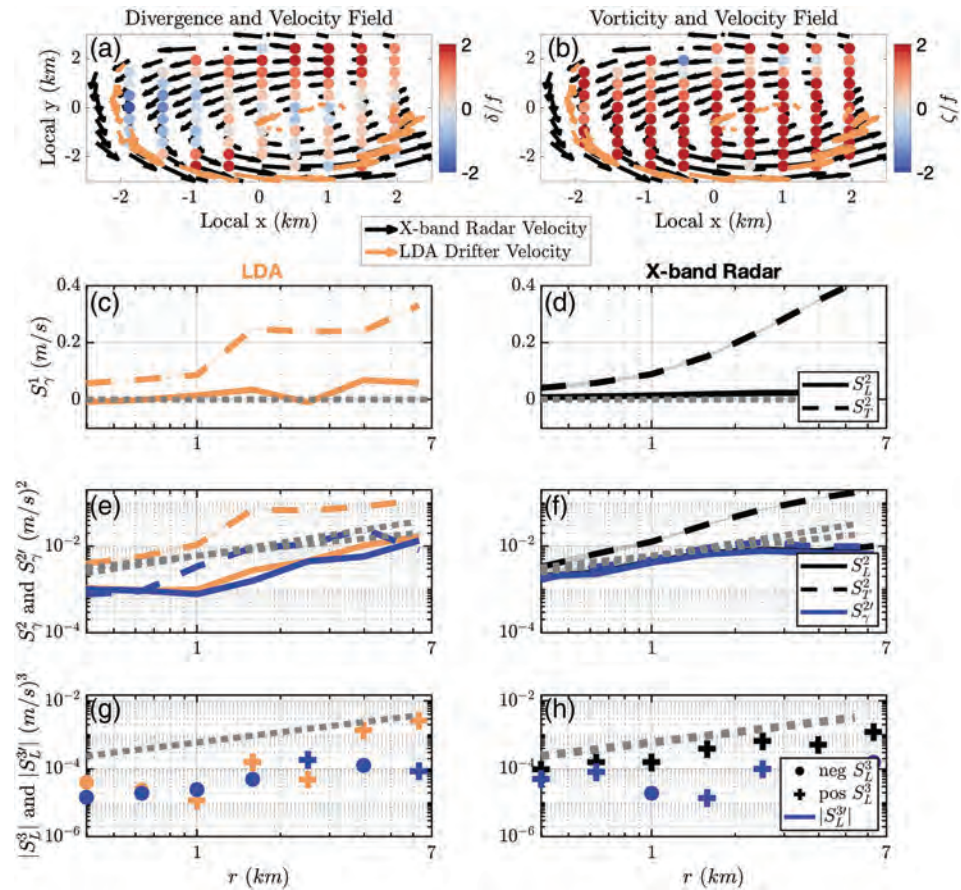


**Figure 8.** Same as Figure 6 but for data from a vortex on 12 February 2016 at 6:00:59 UTC, using LDA drifters instead of P2 & P3 drifters.

for P2 & P3 is shallower. These less than conclusive results limit the utility of using this statistic to diagnose energy flux across scales.

#### 4.3.1. Corrected Third-Order Structure Functions

The corrections to the third-order structure function for the background bias proposed in equation (3) tends to be more substantial than that to the second-order structure function from equation (2), especially at larger scales, because it contains a term proportional to  $S_\gamma^1 S_\gamma^2$ . Consequently, the sign and magnitude of the third-order uncorrected structure function is potentially dependent through background bias on the sign and magnitude of the first-order structure function. The corrected quasi-Lagrangian and Eulerian third-order structure functions,  $S_L^{3'}$ , are presented in Figures 4 and 5, respectively. While the Eulerian  $S_L^3$  does not deviate much from the Eulerian  $S_L^3$  for the P2 & P3 sample, its sign changes for scales above 1.5 km in both the P1 and LDA samples. The quasi-Lagrangian  $S_L^{3'}$  agrees in sign with the uncorrected  $S_L^3$  for all estimates, but the magnitudes are lower for LDA and P2 & P3 (though not for P1) across almost all scales. Nonetheless, the corrected third-order structure functions fall inside the confidence intervals of the uncorrected third-order structure functions for both drifter and X-band data, with the exception of the P2 & P3 drifters, which fall outside across most scales, and P1 which does above 2 km. This is a consequence of the inherent noisiness of higher-order statistics and illustrates the challenges of drawing reliable conclusions from the third-order structure function estimates from noisy observations.

#### 4.3.2. $S_\gamma^3$ as a Function of Divergence and Vorticity

Mirroring the analysis in section 4.2.2, the potential effect of accumulation bias on the third-order structure function is investigated by considering the absolute value of the uncorrected  $S_L^3$  as a function of both scale and divergence ( $S_L^3(r, \Delta)$ ) and then of both scale and vorticity ( $S_L^3(r, \zeta)$ ). See the yellow-blue colored fields in Figures 9a and 9b, respectively. Negative values are marked with black bullets. Overlaid with black-white contours are again the JPDF of scale and divergence (left) and of scale and vorticity (right). The distributions

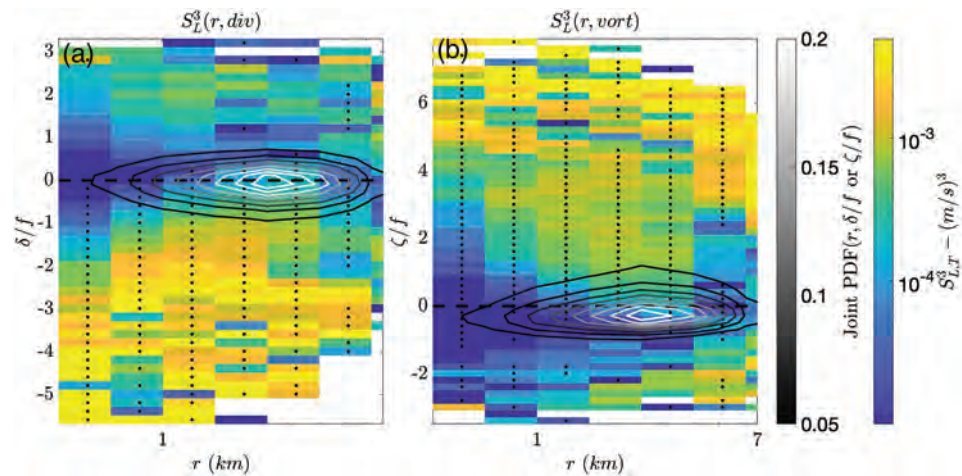


**Figure 9.** The absolute value of the Eulerian longitudinal *uncorrected* third-order structure function dependent on divergence and scale (a) and vorticity and scale (b), denoted by the blue to yellow logarithmic colorbar. Negative values are stippled with a ‘•’ and positive values are left unstippled. The joint probability density function of divergence and separation distance (a) and vorticity and separation distance (b) is shown by contours and the black to white linear colorbar.

are, as expected, noisier than the corresponding results for  $S_L^2$ . Nonetheless, some broad patterns can be discerned. A gradient with respect to  $r$  exists for small values of divergence and vorticity where the bulk of the samples lie. Gradients with respect to  $\Delta$  and  $\zeta$  also exist. Negative values of  $S_L^3$  are associated with negative values of divergence and increase with increasing divergence, becoming positive except for a handful of bins with very high divergence, which are likely not sampled well. The transition point to positive values is scale dependent. With respect to vorticity, negative values of  $S_L^3$  are associated with positive vorticity and  $S_L^3$  increasing as vorticity decreases. The transition to positive values is not as clear. The figure suggests that a disproportionate sampling of large convergence and/or positive vorticity is expected to flatten the slope and increase the magnitude of  $S_L^3(r)$ .

#### 4.3.3. Biases in Third-Order Structure Functions at a Front

The third-order uncorrected and corrected structure functions at a front are plotted in Figures 7g and 7h. Note first that here the drifters and the X-band radar  $S_L^3$  are significantly affected by nonzero  $S_L^1$ , which changes both the sign and magnitude of the third-order structure function across all separation scales. Unlike  $S_L^3$  for the full P2 & P3 data set (cf. Figures 4 and 5), the corrected third-order statistics for this frontal snapshot lie well outside the confidence intervals of the uncorrected  $S_L^3$  across all separations except 1.5 km for the P2 & P3 drifters and at all scales above 1 km for the X-band radar data (not shown). As observed in section 4.3.2, the strong convergence (-2f) and the high vorticity (2f) sampled by the drifters are both associated with a flatter, negative  $S_L^3$ , which is seen in Figure 7g. As with the Eulerian  $S_L^2$ , sampling that is less biased toward high convergence and vorticity results in an  $S_L^3$  that is comparable to that from the full P2 & P3 data set (Figure 5) in slope, although with lower values across all scales.

#### 4.3.4. Biases in Third-Order Structure Functions at a Vortex

The third-order uncorrected and corrected structure functions at a vortex are plotted in Figures 8g and 8h. As with the frontal case, sign and magnitude of both the drifters and the X-band radar  $S_L^3$  are impacted across all separation scales by the correction for nonzero  $S_L^1$ . Additionally, the corrected  $S_L^3$  are outside of the confidence intervals of the uncorrected  $S_L^3$  above 1 km (not shown). As noted in section 4.2.4, the first-order structure functions indicate stronger vorticity and divergence being sampled at larger scales. Unlike for  $S_L^2$ , however, this sampling bias results in contradictory trends in  $S_L^3$ , as shown in Figure 9. The variability, particularly in sign, seen in Figures 8g and 8h may therefore be a consequence of the sampling biases.

## 5. Conclusions

Surface drifters are a powerful observational platform providing high spatial and temporal resolution hard to come by via other instrumentation to assess dispersion of floating material in the ocean. Previous studies suggest a key characteristic is that their sampling pattern is not agnostic to the flow properties, making such a quasi-Lagrangian velocity data set fundamentally different from an Eulerian one. In particular,

Pearson et al. (2019) demonstrate that correlated divergence and vorticity lead to shallower second-order and larger third-order structure functions at scales below 30 km. The second- and third-order structure functions presented here are shallower and larger, respectively, than the corresponding Eulerian statistics, consistent with the results of Pearson et al. (2019). Alongside validating the prevalence of the drifter biases in observations, this study builds upon the work of Pearson et al. (2019) by refining the impacts of convergence and vorticity on the second- and third-order structure functions. The observational analysis highlights that the preferential sampling of convergence regions and areas with strong vorticity results in an *accumulation* bias. Its potential impact on structure function statistics can be determined by considering the statistics computed from an Eulerian velocity field as a function not just of separation scale but also of divergence or vorticity. We found that the steepest gradient as a function of  $r$  is associated with near-zero values of divergence and vorticity, which are also most commonly sampled by the Eulerian X-band radar along the shiptrack in our data. At stronger convergence, the  $S_v^2$  and  $S_L^2$  show shallower slopes, as they increase more at smaller scales. Evidence of this effect is seen in the statistics of data subsampled specifically to coincide with a strong front. Similarly, high positive vorticity tends to increase the magnitudes of the structure functions and flatten them. This tendency can be identified in data subsampled in a strong vortex.

In classic turbulence theory, the flow is assumed to be statistically isotropic and homogeneous, so that the first-order structure function is zero for all scales. However, this assumption does not hold in either the quasi-Lagrangian or the Eulerian observational data. This raises the question whether second- and third-order structure functions should be computed after the mean flow has been removed. Such a correction for *background* bias can have a great impact on the statistics. In particular, the sign and magnitude of the third-order structure function can be driven by the sign and magnitude of the first-order structure function, not the perturbations that are related to energy transfer across scales. The effect is smaller in the Eulerian data when sampled over a sufficiently large domain.

The sizable influence of these biases on the structure function statistics demonstrates that any interpretation or comparison must take the sampling schemes into account. In particular, it may not be appropriate to attempt to link third-order structure functions to energy fluxes, especially when based on drifter data that is almost invariably subject to both background and accumulation biases. While Eulerian measurements can be flow independent by design, they, too, may be subject to background and sampling representativeness biases akin to accumulation biases, requiring caution even when deriving statistics from them.

## Data Availability Statement

Data are publicly available through the Gulf of Mexico Research Initiative Information & Data Cooperative (GRIIDC) at <https://data.gulfresearchinitiative.org> under DOIs 10.7266/N7N01550 (X-band radar) and 10.7266/N7W0940J (drifters).

## Acknowledgments

The authors wish to thank the large team of scientists and support staff during the LASER campaign. This research was made possible in part by a grant from The Gulf of Mexico Research Initiative to the Consortium for Advanced Research on the Transport of Hydrocarbons in the Environment (CARTHE) and in part by Grant N00014-17-1-2963 from the Office of Naval Research.

## References

- Babiano, A., Basdevant, C., & Sadourny, R. (1985). Structure functions and dispersion laws in two-dimensional turbulence. *Journal of the Atmospheric Sciences*, *42*(9), 941–949.
- Barrick, D. E., & Peake, W. H. (1968). A review of scattering from surfaces with different roughness scales. *Radio Science*, *3*(8), 865–868.
- Bennett, A. (1984). Relative dispersion: Local and nonlocal dynamics. *Journal of the Atmospheric Sciences*, *41*(11), 1881–1886.
- Braun, N., Ziemer, F., Bezuglov, A., Cysewski, M., & Schymura, G. (2008). Sea-surface current features observed by Doppler radar. *IEEE Transactions on Geoscience and Remote Sensing*, *46*(4), 1125–1133. <https://doi.org/10.1109/TGRS.2007.910221>
- Buckingham, C. E., Naveira Garabato, A. C., Thompson, A. F., Brannigan, L., Lazar, A., Marshall, D. P., et al. (2016). Seasonality of submesoscale flows in the ocean surface boundary layer. *Geophysical Research Letters*, *43*, 2118–2126. <https://doi.org/10.1002/2016GL068009>
- Callies, J., & Ferrari, R. (2013). Interpreting energy and tracer spectra of upper-ocean turbulence in the submesoscale range (1–200 km). *Journal of Physical Oceanography*, *43*(11), 2456–2474.
- Callies, J., Ferrari, R., Klymak, J. M., & Gula, J. (2015). Seasonality in submesoscale turbulence. *Nature Communications*, *6*, 6862.
- Campana, J., Terrill, E. J., & de Paolo, T. (2017). A new inversion method to obtain upper-ocean current-depth profiles using X-band observations of deep-water waves. *Journal of Atmospheric and Oceanic Technology*, *34*(5), 957–970.
- Capet, X., Campos, E., & Paiva, A. (2008). Submesoscale activity over the Argentinian shelf. *Geophysical Research Letters*, *35*, L15605. <https://doi.org/10.1029/2008GL034736>
- Capet, X., McWilliams, J. C., Molemaker, M. J., & Shchepetkin, A. (2008). Mesoscale to submesoscale transition in the California Current System. Part I: Flow structure, eddy flux, and observational tests. *Journal of Physical Oceanography*, *38*(1), 29–43.
- Capet, X., McWilliams, J. C., Molemaker, M. J., & Shchepetkin, A. (2008). Mesoscale to submesoscale transition in the California Current System. Part III: Energy balance and flux. *Journal of Physical Oceanography*, *38*(10), 2256–2269.
- Chang, H., Huntley, H. S., Jr, A. K., Carlson, D. F., Mensa, J. A., Mehta, S., et al. (2019). Small-scale dispersion in the presence of Langmuir circulation. *Journal of Physical Oceanography*, *49*(12), 3069–3085.

- Choi, J., Bracco, A., Barkan, R., Shchepetkin, A. F., McWilliams, J. C., & Molemaker, J. M. (2017). Submesoscale dynamics in the northern Gulf of Mexico. Part III: Lagrangian implications. *Journal of Physical Oceanography*, *47*(9), 2361–2376.
- D'Asaro, E., Lee, C., Rainville, L., Harcourt, R., & Thomas, L. (2011). Enhanced turbulence and energy dissipation at ocean fronts. *Science*, *332*(6027), 318–322.
- D'Asaro, E. A., Shcherbina, A. Y., Klymak, J. M., Molemaker, J., Novelli, G., Guigand, C. M., et al. (2018). Ocean convergence and the dispersion of floats. *Proceedings of the National Academy of Sciences of the United States of America*, *115*(6), 1162.
- Davis, R. E. (1991). Observing the general circulation with floats. *Deep Sea Research*, *38*, S531–S571.
- Du Plessis, M., Swart, S., Anson, I. J., Mahadevan, A., & Thompson, A. F. (2019). Southern ocean seasonal restratification delayed by submesoscale wind-front interactions. *Journal of Physical Oceanography*, *49*, 1035–1053.
- Fox-Kemper, B., Danabasoglu, G., Ferrari, R., Griffies, S. M., Hallberg, R. W., Holland, M. M., et al. (2011). Parameterization of mixed layer eddies. III: Implementation and impact in global ocean climate simulations. *Ocean Modelling*, *39*(1–2), 61–78.
- Frehlich, R., & Sharman, R. (2010). Climatology of velocity and temperature turbulence statistics determined from rawinsonde and ACARS/AMDAR data. *Journal of Applied Meteorology and Climatology*, *49*(6), 1149–1169.
- Frisch, U. (1995). *Turbulence: The legacy of A. N. Kolmogorov*. Cambridge: Cambridge University Press.
- Griffa, A., Lumpkin, R., & Veneziani, M. (2008). Cyclonic and anticyclonic motion in the upper ocean. *Geophysical Research Letters*, *35*, L01608. <https://doi.org/10.1029/2007GL032100>
- Haza, A. C., D'Asaro, E., Chang, H., Chen, S., Curcic, M., Guigand, C., et al. (2018). Drogue-loss detection for surface drifters during the Lagrangian Submesoscale Experiment (LASER). *Journal of Atmospheric and Oceanic Technology*, *35*(4), 705–725.
- Johnson, L., Lee, C. M., & D'Asaro, E. A. (2016). Global estimates of lateral springtime restratification. *Journal of Physical Oceanography*, *46*(5), 1555–1573.
- Klein, P., & Lapeyre, G. (2009). The oceanic vertical pump induced by mesoscale and submesoscale turbulence. *Annual Review of Marine Science*, *1*, 351–375.
- Kolmogorov, A. N. (1941). The local structure of turbulence in incompressible viscous fluid for very large Reynolds numbers. *Cr Acad. Sci. URSS*, *30*, 301–305.
- LaCasce, J. H. (2008). Statistics from Lagrangian observations. *Progress in Oceanography*, *77*(1), 1–29. <https://doi.org/10.1016/j.pocean.2008.02.002>
- LaCasce, J. (2016). Estimating Eulerian energy spectra from drifters. *Fluids*, *1*(4), 33.
- Li, Q. P., Franks, P. J., Ohman, M. D., & Landry, M. R. (2012). Enhanced nitrate fluxes and biological processes at a frontal zone in the southern California current system. *Journal of Plankton Research*, *34*(9), 790–801.
- Lindborg, E. (1999). Can the atmospheric kinetic energy spectrum be explained by two-dimensional turbulence? *Journal of Fluid Mechanics*, *388*, 259–288.
- Lindborg, E. (2007). Third-order structure function relations for quasi-geostrophic turbulence. *Journal of Fluid Mechanics*, *572*, 255–260.
- Lund, B., Graber, H. C., Tamura, H., Collins III, C. O., & Varlamov, S. M. (2015). A new technique for the retrieval of near-surface vertical current shear from marine X-band radar images. *Journal of Geophysical Research: Oceans*, *120*, 8466–8486. <https://doi.org/10.1002/2015JC010961>
- Lund, B., Haus, B. K., Horstmann, J., Graber, H. C., Carrasco, R., Laxague, Nathan J. M., et al. (2018). Near-surface current mapping by shipboard marine x-band radar: A validation. *Journal of Atmospheric and Oceanic Technology*, *35*(5), 1077–1090. <https://doi.org/10.1175/JTECH-D-17-0154.1>
- Luo, H., Bracco, A., Cardona, Y., & McWilliams, J. C. (2016). Submesoscale circulation in the northern Gulf of Mexico: Surface processes and the impact of the freshwater river input. *Ocean Modelling*, *101*, 68–82.
- Lyzenga, D. R., & Walker, D. T. (2015). A simple model for marine radar images of the ocean surface. *IEEE Geoscience and Remote Sensing Society*, *12*(12), 2389–2392.
- Mahadevan, A., & Tandon, A. (2006). An analysis of mechanisms for submesoscale vertical motion at ocean fronts. *Ocean Modelling*, *14*(3–4), 241–256.
- McCaffrey, K., Fox-Kemper, B., & Forget, G. (2015). Estimates of ocean macroturbulence: Structure function and spectral slope from Argo profiling floats. *Journal of Physical Oceanography*, *45*, 1773–1793.
- McCaffrey, K., Fox-Kemper, B., Hamlington, P. E., & Thomson, J. (2015). Characterization of turbulence anisotropy, coherence, and intermittency at a prospective tidal energy site: Observational data analysis. *Renewable Energy*, *76*, 441–453.
- McWilliams, J. C. (2008). Fluid dynamics at the margin of rotational control. *Environmental Fluid Mechanics*, *8*(5–6), 441–449.
- McWilliams, J. C. (2016). Submesoscale currents in the ocean. *Proceedings of the Royal Society of London. Series A*, *472*(2189), 20160117.
- McWilliams, J. C., Molemaker, J., & Yavneh, I. (2001). From stirring to mixing of momentum: Cascades from balanced flows to dissipation in the oceanic interior: California Univ. Los Angeles Inst. of Geophysics and Planetary Physics.
- Molemaker, M. J., McWilliams, J. C., & Yavneh, I. (2005). Baroclinic instability and loss of balance. *Journal of Physical Oceanography*, *35*(9), 1505–1517.
- Nieto Borge, J. C., Rodríguez Rodríguez, G., Hessner, K., & Izquierdo González, P. (2004). Inversion of marine radar images for surface wave analysis. *Journal of Atmospheric and Oceanic Technology*, *21*(8), 1291–1300.
- Novelli, G., Guigand, Cédric M., Cousin, C., Ryan, E. H., Laxague, Nathan J. M., Dai, H., et al. (2017). A biodegradable surface drifter for ocean sampling on a massive scale. *Journal of Atmospheric and Oceanic Technology*, *34*(11), 2509–2532.
- Ohlmann, J., Molemaker, M., Baschek, B., Holt, B., Marmorino, G., & Smith, G. (2017). Drifter observations of submesoscale flow kinematics in the coastal ocean. *Geophysical Research Letters*, *44*, 330–337. <https://doi.org/10.1002/2016GL071537>
- Omand, M. M., D'Asaro, E. A., Lee, C. M., Perry, M. J., Briggs, N., Cetinić, I., & Mahadevan, A. (2015). Eddy-driven subduction exports particulate organic carbon from the spring bloom. *Science*, *348*(6231), 222–225.
- Pearson, J., Fox-Kemper, B., Barkan, R., Choi, J., Bracco, A., & McWilliams, J. C. (2019). Impacts of convergence on structure functions from surface drifters in the Gulf of Mexico. *Journal of Physical Oceanography*, *49*(3), 675–690.
- Poje, A. C., Özgökmen, T. M., Bogucki, D. J., & Kirwan, A. D. (2017). Evidence of a forward energy cascade and Kolmogorov self-similarity in submesoscale ocean surface drifter observations. *Physics of Fluids*, *29*(2), 020,701.
- Poje, A. C., Özgökmen, T. M., Lipphardt, B. L., Haus, B. K., Ryan, E. H., Haza, A. C., et al. (2014). Submesoscale dispersion in the vicinity of the Deepwater Horizon spill. *Proceedings of the National Academy of Sciences of the United States of America*, *111*(35), 12,693.
- Riser, S. C. (1982). The quasi-Lagrangian nature of SOFAR floats. *Deep Sea Research*, *29*(12), 1587–1602.
- Senet, C. M., Seemann, J., & Ziemer, F. (2001). The near-surface current velocity determined from image sequences of the sea surface. *IEEE Transactions on Geoscience and Remote Sensing*, *39*(3), 492–505.
- Stewart, R. H., & Joy, J. W. (1974). HF radio measurements of surface currents. *Deep Sea Research*, *21*(12), 1039–1049.

- Stole-Hentschel, S., Seemann, J., Nieto Borge, J. C., & Trulsen, K. (2018). Consistency between sea surface reconstructions from nautical X-band radar doppler and amplitude measurements. *Journal of Atmospheric and Oceanic Technology*, 35(6), 1201–1220.
- Thomas, L. N., Tandon, A., & Mahadevan, A. (2008). Submesoscale processes and dynamics, *Ocean modeling in an eddying regime* (pp. 17–38): American Geophysical Union (AGU).
- Trizna, D. B., Hansen, J. P., Hwang, P., & Wu, J. (1991). Laboratory studies of radar sea spikes at low grazing angles. *Journal of Geophysical Research*, 96(C7), 12,529–12,537.
- Webb, E. K. (1964). Ratio of spectrum and structure-function constants in the inertial subrange. *Quarterly Journal of the Royal Meteorological Society*, 90(385), 344–346. <https://doi.org/10.1002/qj.49709038520>
- Wetzel, L. B. (1990). *Surface waves and fluxes*. In G. L. Geernaert, & W. J. Plant (eds.). (pp. 109–171). Dordrecht, the Netherlands: Kluwer.
- Wright, J. (1968). A new model for sea clutter. *IEEE Transactions on Antennas and Propagation*, 16(2), 217–223.
- Yaremchuk, M., & Coelho, E. F. (2015). Filtering drifter trajectories sampled at submesoscale resolution. *IEEE Journal of Oceanic Engineering*, 40(3), 497–505. <https://doi.org/10.1109/JOE.2014.2353472>
- Young, I. R., Rosenthal, W., & Ziemer, F. (1985). A three-dimensional analysis of marine radar images for the determination of ocean wave directionality and surface currents. *Journal of Geophysical Research*, 90(C1), 1049–1059.
- Zhong, Y., Bracco, A., & Villareal, T. A. (2012). Pattern formation at the ocean surface: Sargassum distribution and the role of the eddy field. *Limnology and Oceanography*, 2(1), 12–27.